ADVANCED PHOTONICS RESEARCH
Open Access
www.adpr-journal.com

Imaging Photonic Resonances within an All-Dielectric Metasurface via Photoelectron Emission Microscopy

*Andrew R. Kim, Chloe F. Doiron, Fernando J. Vega, Jaeyeon Yu, Alex M. Boehm, Joseph P. Klesko, Igal Brener, Raktim Sarma, Alexander Cerjan, and Taisuke Ohta**

Dielectric metasurfaces, through volume-type photonic resonances, enable precise control of light-matter interactions for applications including imaging, holography, and sensing. The application space of dielectric metasurfaces has extended from infrared to visible wavelengths by incorporating high refractive index materials, such as titanium dioxide (TiO_2). Understanding the fundamental and fabrication limits for these applications requires metrology with nanoscale resolution, sensitivity to electromagnetic fields within the meta-atom volume, and far-field excitation. In this work, photoelectron emission microscopy (PEEM) is used to image field distributions of photonic resonances in a TiO_2 metasurface excited with far-field, visible-wavelength illumination. The local volumetric field variations within the meta-atoms are analyzed as a function of illumination angle and polarization by comparing photoelectron images to finite-difference time-domain simulations. This study determines the inelastic mean free path of very low-energy (<1 eV) photoelectrons to be 35 ± 10 nm, which is comparable to the meta-atom height thereby highlighting PEEM sensitivity to resonances within the volume. Additionally, the simulations reveal high sensitivity of PEEM images to an in-plane component of the illumination *k*-vector. These results demonstrate that photoelectron imaging with subwavelength resolution offers unique advantages for examining light-matter interactions in volume-type (as opposed to surface) photonic modes within dielectric nanophotonic structures.

1. Introduction

Precise control of light-matter interactions can be achieved using resonant optical devices, such as metasurfaces[1–4] and photonic crystals.[5,6] These structural motifs are deployed in applications including sensing,[7,8] imaging,[9–11] holography,[12–14] phase control optics,[15,16] and nonlinear optics.[17,18] By utilizing materials with high refractive indexes,[19] such as titanium dioxide (TiO_2), dielectric metasurfaces have extended their application space from the infrared wavelength to the visible range.[20,21] Moreover, the design of dielectric metasurfaces has achieved remarkable advances in engineering nanoresonators (i.e., meta-atoms) that confine light to increasingly smaller length scales that are shorter than the excitation optical wavelength. Consequently, understanding the fundamental and fabrication limitations of metasurface designs requires direct imaging of electromagnetic fields that dictate the light-matter interactions within the meta-atoms. As the overall optical response of the metasurface can be tailored by exploiting[8,22–25] or breaking[26,27] the system's spatial symmetry and periodicity, it is important to elucidate the relationship between the symmetry of the resonance and the polarization and incident configuration of the illuminating light (i.e., *k*-vector). Thus, metrology and characterization of dielectric nanophotonic structures require an imaging approach with nanoscale resolution, sensitivity to the electromagnetic fields within the volume of the meta-atoms, and far-field excitation to control the polarization and incident configuration.

Photoelectron emission microscopy (PEEM) is one approach for imaging local field distributions of resonances within dielectric metasurfaces with far-field illumination at suboptical-wavelength resolution.[28,29] The far-field illumination offers control over the illumination *k*-vector, to which metasurfaces are sensitive,[30–32] in addition to polarization and wavelength. Its large illumination area can coherently excite multiple meta-atoms in a metasurface to investigate nonlocal, collective resonances[33–36] and concurrently excite local, site-specific phenomena. Importantly, the use of far-field illumination replicates the illumination conditions in common applications of nanophotonic devices, distinguishing PEEM from other nanoscale electric

A. R. Kim, C. F. Doiron, F. J. Vega, J. Yu, A. M. Boehm, J. P. Klesko, I. Brener, R. Sarma, A. Cerjan, T. Ohta
Sandia National Laboratories
1515 Eubank Blvd SE, Albuquerque, NM 87185, USA
E-mail: tohta@sandia.gov

C. F. Doiron, J. Yu, I. Brener, R. Sarma, A. Cerjan
Center for Integrated Nanotechnologies
Sandia National Laboratories
1515 Eubank Blvd SE, Albuquerque, NM 87185, USA

F. J. Vega
School of Mechanical Engineering
Purdue University
585 Purdue Mall, West Lafayette, IN 47907, USA

The ORCID identification number(s) for the author(s) of this article can be found under https://doi.org/10.1002/adpr.202400223.

© 2025 The Author(s). Advanced Photonics Research published by Wiley-VCH GmbH. This is an open access article under the terms of the Creative Commons Attribution License, which permits use, distribution and reproduction in any medium, provided the original work is properly cited.

DOI: 10.1002/adpr.202400223

26999293, 2025, 6, Downloaded from https://advanced.onlinelibrary.wiley.com/doi/10.1002/adpr.202400223 by Sandia National Laboratory, Wiley Online Library on [12/06/2025]. See the Terms and Conditions (https://onlinelibrary.wiley.com/terms-and-conditions) on Wiley Online Library for rules of use; OA articles are governed by the applicable Creative Commons License

field imaging approaches that can improve metasurface design and diagnostics. The de Broglie wavelength of the photoelectrons generated by the metasurface provides suboptical-wavelength spatial resolution.[37] Altogether, these factors give PEEM unique advantages toward imaging nanophotonic systems to complement other near-field techniques (e.g., cathodoluminescence,[38–40] electron energy loss spectroscopy,[40,41] and scanning near-field optical microscopy[42,43]) and have been utilized to advance PEEM imaging of plasmonic resonances on metallic nanostructures with exquisite control of polarization and wavefront.[44–53]

Presently, connecting PEEM images of dielectric metasurfaces to the local resonant field distributions is challenging due to the undetermined inelastic mean free path (IMFP) of the very low kinetic energy (<1 eV) photoelectrons. An estimate of the IMFP is required to quantify the sampling depth of PEEM, since the photoelectrons produced within the volume of the meta-atoms must travel toward the surface to eventually be emitted to vacuum. The electron IMFP as a function of electron energy is usually described by the "universal curve", which is well corroborated experimentally for electrons with 10–100 eV or greater.[54,55] In contrast, the validity of the universal curve is less certain for electrons of very low kinetic energy (<1 eV), the energy scale comparable to phonons and other many-body interactions in materials[56] and barely enough to overcome the material work function. For metals, both calculations[57–60] and experimental data[60–63] show that the IMFP ranges within 3–10 nm. Dielectric materials appear to show larger IMFP values in the 10–100 nm range suggested by calculations,[64–66] but these values are not experimentally verified to our knowledge.[67,68] To address this uncertainty of IMFP for very low kinetic energy electrons and to validate the applicability of PEEM to dielectric photonic systems beyond depth-independent phenomena,[28,29] an empirical determination of the IMFP is essential.

In this article, we use PEEM in conjunction with finite-difference time-domain (FDTD) simulation to evaluate the electromagnetic field distribution of the photonic resonances of a TiO_2 metasurface as a function of input polarization and excitation photon energy (E_{ph}) across the ultraviolet (UV) to visible range. The E_{ph} range is chosen to be beneath the threshold for electronic excitations of TiO_2 such that two-photon photoemission (2PPE) processes probe the impact of photonic resonances alone. The metasurface is designed to support Fabry–Pérot (FP) and Fano resonances that overlap in E_{ph} and shift their intensity between two distinct areas, that is, interior and exterior of the meta-atom. Because the two areas have different TiO_2 thicknesses and attenuate photoelectrons differently, we exploit the contrast in PEEM intensity as E_{ph} is varied to estimate the IMFP in TiO_2. Using an iterative approach to match the intensity distribution in the simulated images to that of PEEM images, we determine the very low kinetic energy electron IMFP of 35 ± 10 nm. This IMFP is comparable to the height of the meta-atoms and ensures the sensitivity of PEEM to resonances within the meta-atom volume. Additionally, the simulations reveal that PEEM images are sensitive to slightly off-normal illumination that introduces an in-plane component of the illumination k-vector, an effect not previously elaborated in PEEM studies.[35] Altogether, our work demonstrates subwavelength PEEM imaging of volume-type photonic resonances supported by the metasurface and suggests the sizable probing depth applicable to other dielectric systems.

2. Results and Discussion

An illustration of how PEEM images the photonic modes excited in the TiO_2 metasurface is shown in **Figure 1**a. A square lattice array of TiO_2 meta-atoms (cylindrical resonators) is illuminated by a collimated far-field optical source at near-normal incidence (not to scale). The illuminating laser, which is ≈100 μm in diameter and has a full width at half maximum of ≈1% of the central wavelength, coherently excites many of the meta-atoms simultaneously to enable study of their collective behavior. The resulting electric fields within the host material excite electrons above the vacuum level via the photoelectric effect, with higher field intensity resulting in a greater number of photoemitted electrons.[69] The emitted photoelectrons, whose de Broglie wavelength provides high spatial resolution (10–20 nm),[37] are directed onto an electron detector via electron optics that preserve their spatial origin. By scanning across excitation wavelengths, a series of photoelectron images are acquired and compiled into a "spectral hypercube data set" that contains the photoelectron yield spectra (analogous to optical absorption spectra) as a function of location across the sample. Here, if the incident wavelength falls within the bandwidth of one or more resonances, light will couple to those resonances. To investigate how the spectra and spatial distribution of the photonic resonances depend on the input polarization, the dataset is acquired for different polarizations of light as defined in Figure 1b, where red arrows represent the direction of polarization in a top-down view of the meta-atoms. Since the metasurface is sensitive to the incident configuration of the illuminating light, we describe small deviations of the k-vector of the light from normal incidence using the polar angle θ and azimuthal angle φ, defined in Figure 1c.

The designed dimensions of the TiO_2 metasurface on a fused silica substrate are provided in Figure 1d, with a unit cell size of 300 nm, meta-atom diameter of 200 nm, and meta-atom height of 75 nm. Because the meta-atoms sit on an insulating SiO_2 substrate, an additional 10 nm of TiO_2 was deposited over the entire surface via atomic layer deposition (ALD) to avoid sample charging (see Sample Fabrication in Section 4). The additional TiO_2 is not different from the TiO_2 of the meta-atoms in terms of their material properties but alters the detailed dimension of the meta-atom within the unit cell to include a thin layer of TiO_2 in the area exterior (denoted in Figure 1d) to the meta-atom. The overall geometry of the TiO_2 metasurface is captured in the scanning electron micrograph shown in Figure 1e. To reduce the impact of imperfections in the individual meta-atoms, PEEM images average over 36 unit cells. To minimize the effect of the broken translational symmetry at the array edges, the averaging was limited to unit cells at least 8 cells away from the edge.[29] See the "PEEM Data Processing" section in Supporting Information for details.

The photoemission process excites electrons in occupied electronic states above the vacuum level. Because the designed resonances of the metasurface are within the visible E_{ph} range, photoelectron excitation requires multiphoton absorption shown in Figure 1f. The density of occupied states of TiO_2 is illustrated

© 2025 The Author(s). Advanced Photonics Research published by Wiley-VCH GmbH

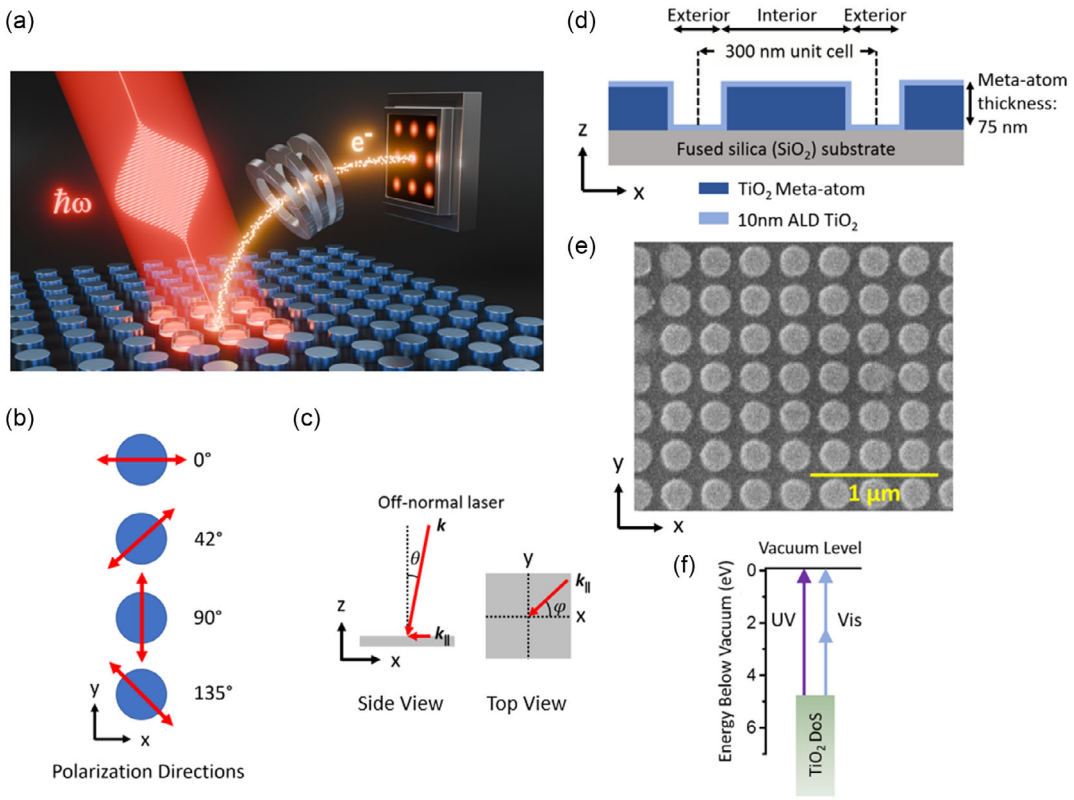


Figure 1. PEEM measurement geometry, TiO_2 metasurface sample, and electronic levels involved in the photoemission process (not to scale). a) The metasurface is illuminated by photons in the UV–vis range with a predetermined polarization at near-normal incidence. The resulting photoelectrons are directed by electron optics to a detector for imaging. b) Definition of the four light polarizations used in this study, with the red arrows representing the polarization directions. c) The incident light can be slightly off normal incidence. Its polar (θ) and azimuthal (φ) angles with respect to the surface normal are defined with respect to Cartesian coordinates. d) Cross-sectional view of the metasurface, showing the designed physical dimensions. e) Scanning electron micrograph of the metasurface. In (a–e), the *x*- and *y*-directions are in-plane with the sample surface, and *z*-direction is the sample normal. f) Electron energy diagram of the photoemission process for TiO_2, showing that the visible wavelength illumination results in two-photon photoemission excited from its occupied density of states (DoS).

by the green rectangle, and the energy supplied by the deep UV–vis light is represented by the purple and light blue arrows, respectively. As the central resonance frequencies of the metasurface fall within the visible wavelength range (2.5 eV (500 nm) to 3.1 eV (400 nm)), two-photon photoemission (2PPE) overcomes the ≈4.9 eV work function of TiO_2 (see Figure S1a, Supporting Information). Below 2.5 eV excitation, 2PPE becomes very inefficient.[70,71] The resonant wavelength is designed such that the photon energy is below the electronic band gap of TiO_2 (3.0–3.2 eV),[72,73] thereby avoiding electronic transitions. Since 2PPE intensity is enhanced proportionally to the fourth power of the electromagnetic field, that is, $|\boldsymbol{E}|^4$,[48,74,75] the PEEM images formed from this process are nonlinear maps of the near-field distribution of the metasurface's optical response.

We performed the FDTD simulations using the package MIT Electromagnetic Equation Propagation (MEEP)[76] to analyze the PEEM images. The simulations compute the $|\boldsymbol{E}|^4$ distribution to represent the 2PPE-PEEM intensity distribution. Since the photonic resonances in the dielectric metasurface exist within the volume of the meta-atom, the simulation integrates the $|\boldsymbol{E}|^4$ distribution weighted by the depth-dependent photoelectron attenuation governed by IMFP to produce the final 2D (*x*–*y* plane) image analogous to the PEEM image. A visual representation of the integration is depicted in **Figure 2**. Figure 2a shows diagrams (not to scale) of the unit cell of the metasurface, where (i) is the top view defining the interior (white region) and exterior (dark region) and (ii) is the 3D model. Figure 2b illustrates the integration process, where the unit cell is "sliced" into multiple *x*–*y* planes along the *z*-axis. The red, dashed lines in Figure 2a(ii) highlight the sections of the model corresponding to the top and bottom slices in Figure 2b. Each slice is processed pixel by pixel according to the following rules: 1) If a pixel is located within a vacuum, its intensity is zero. 2) If a pixel is located within some material (TiO_2 meta-atom, exterior TiO_2 layer, or SiO_2 substrate), its intensity I is calculated according to the relationship, $I(D) \propto e^{-D/\lambda}$, where D is the pixel's distance below the surface, and λ is the electron IMFP. Figure 2c illustrates the intensity attenuation as a function of depth (normalized to IMFP) below the surface. The slices are then added together and smoothed spatially with a Gaussian function (lateral sampling distance of 25 nm that corresponds to the approximate pixel size of

© 2025 The Author(s). Advanced Photonics Research published by Wiley-VCH GmbH

26999293, 2025, 6, Downloaded from https://advanced.onlinelibrary.wiley.com/doi/10.1002/adpr.202400223 by Sandia National Laboratory, Wiley Online Library on [12/06/2025]. See the Terms and Conditions (https://onlinelibrary.wiley.com/terms-and-conditions) on Wiley Online Library for rules of use; OA articles are governed by the applicable Creative Commons License

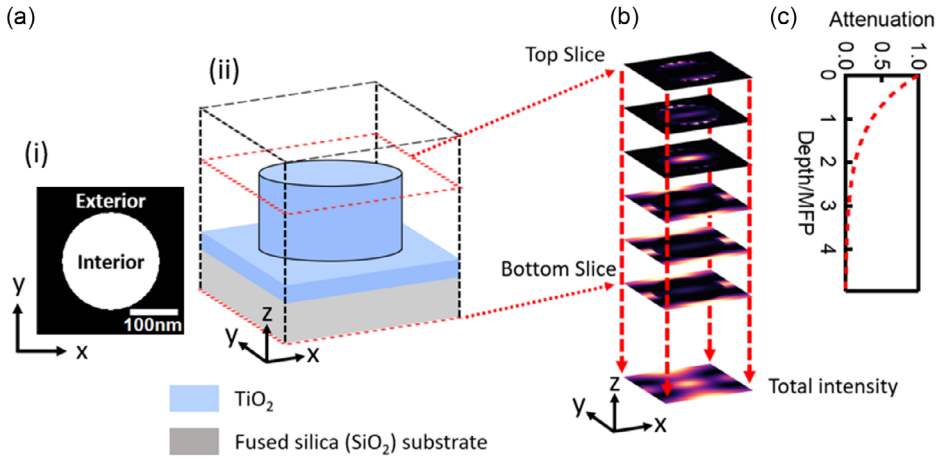


Figure 2. Diagram (not to scale) showing how the field intensity maps are calculated in MEEP simulations with respect to the metasurface geometry. a) Diagram of the unit cell defining the interior and exterior of the meta-atom as shown by (i) top view and (ii) 3D model of the unit cell volume. The dashed, black lines mark the unit cell boundary. b) The field distribution within the unit cell volume is "sliced" into *x*–*y* planes at various heights. The field intensity is removed in areas corresponding to vacuum. c) Plot of field intensity attenuation as a function of depth with respect to the surface directly above. This attenuation is applied to each pixel in each slice in (b), and then, the slices are summed and Gaussian-smoothed to form the final, total field intensity map.

PEEM images). The resulting final image represents the total photoemission intensity that accounts for the effect of IMFP on every photoemitting point within the metasurface. For details describing the MEEP simulations and the parameters to model the experimental setup, including the illuminating light source, metasurface geometry, and metasurface imperfections, see the "MEEP Simulation" and "MEEP Parameters" sections in Supporting Information.

Because the IMFP is unknown a priori, producing a simulated image to match a PEEM image is carried out in an iterative manner. This process involves comparing intensities between regions of different TiO_2 thicknesses (interior versus exterior of meta-atom) in the PEEM and simulated images as the two resonances shift their relative intensities between the regions. We note that the SiO_2 substrate has negligible impact because it has a much lower photoemission yield compared to TiO_2 (see Figure S2, Supporting Information). The comparison is performed for various values of IMFP used to weigh the integration (as described in Figure 2) to determine the appropriate IMFP and reproduce the spatial intensity profile of PEEM images. The simulated images undergo continued iteration until the simulated resonant intensity profile is within 20% of the PEEM image intensity profile. Thus, the simulated images presented in this manuscript are the optimized, integrated images using an IMFP of 35 nm.

We present the results in the subsections that follow: 1) measurement of far-field and PEEM spectra to verify the overlap of the two resonances; 2) comparison of the simulated and PEEM images demonstrating the intensity switching between the interior and exterior of the meta-atom; 3) evaluation of the impact of the illuminating *k*-vector in the simulated and PEEM images; and 4) estimation of the IMFP by leveraging the regions with different TiO_2 thicknesses and optical resonances.

2.1. Overlapping Fabry–Pérot and Fano Resonances in Far-Field and PEEM Spectra

To determine the wavelengths of the designed photonic resonances, we first characterized the TiO_2 metasurface using far-field reflectivity and transmissivity measurements (see Linear Measurements in Section 4). The reflection and transmission spectra of the metasurface are shown in **Figure 3**a by the solid and dashed curves. The designed resonances appear as overlapping peaks (dips) in the reflection (transmission) spectrum as marked by the arrows at ≈2.73 eV (appearing as a shoulder due to the overlap) and ≈2.76 eV. The corresponding spectra acquired using PEEM are shown in Figure 3b for the four polarizations defined in Figure 1b. Each spectrum is obtained by integrating photoemission intensity across multiple meta-atoms in the PEEM images at each E_{ph} to compare with the far-field reflectivity and transmissivity measurements having large probe size that averages over multiple meta-atoms. Note that the PEEM spectra are offset vertically for clarity and normalized to the peak photoemission intensity. All four PEEM spectra show the prominent peak at 2.76 eV that are in good agreement with the resonance peak (dip) at the same E_{ph} in the reflection (transmission) spectrum in Figure 3a. The 2.73 eV shoulder is heavily suppressed in the PEEM spectra, meaning that the field enhancement of this resonance to the 2PPE process is weaker than that of the 2.76 eV peak. A likely reason for the suppression is the nonlinear relationship between the electric field and photoelectron intensity of the two-photon process. An additional reason is that the reflection spectrum measures the electric field that escapes to the far field and does not necessarily measure the field intensity or absorption inside the metasurface. These results suggest that the PEEM spectra do not directly correspond to the far-field linear measurements but rather represent the field enhancements within the meta-atoms by the photonic

© 2025 The Author(s). Advanced Photonics Research published by Wiley-VCH GmbH

26999293, 2025, 6, Downloaded from https://advanced.onlinelibrary.wiley.com/doi/10.1002/adpr.202400223 by Sandia National Laboratory, Wiley Online Library on [12/06/2025]. See the Terms and Conditions (https://onlinelibrary.wiley.com/terms-and-conditions) on Wiley Online Library for rules of use; OA articles are governed by the applicable Creative Commons License

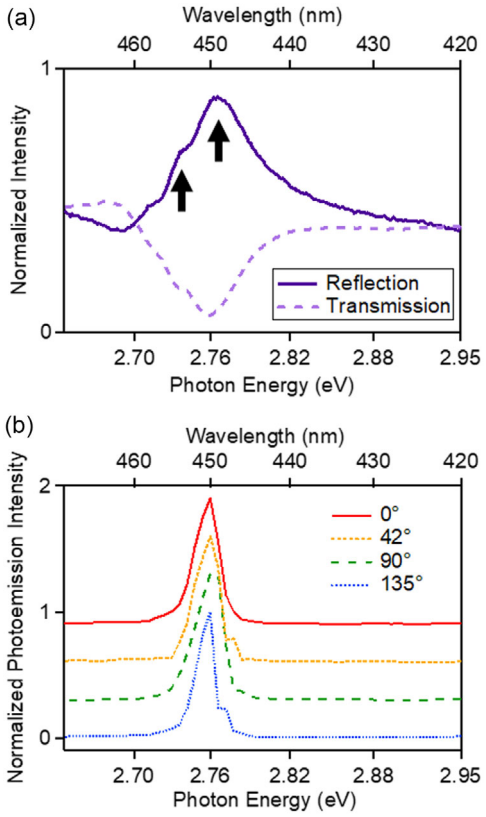


Figure 3. Linear spectra of the metasurface as a function of photon energy from a) reflectivity and transmissivity measurements and b) PEEM image intensity of one unit cell for each of the four polarization angles. All PEEM polarization spectra except 135° are offset vertically for visual clarity. Each PEEM spectrum is corrected for the laser power and 2PPE yield as well as normalized such that the intensity at resonance is 1. The reflectivity and transmissivity spectra are normalized as the fraction of the total incident light. The arrows in (a) point to the two closely overlapping resonance peaks in the reflectivity spectrum.

resonances of the metasurface. Nevertheless, we find a reasonable agreement between the far-field reflectivity and transmissivity measurements and the PEEM spectra.

2.2. Intensity Switching between Exterior and Interior of the Meta-Atoms

Next, we investigate the spatial profile of the photonic modes contributing to the resonant peaks in Figure 3b by examining the spatial distribution of photoemission intensity as a function of E_{ph}. PEEM images of one unit cell of the metasurface are presented in **Figure 4**a,b for 0° and 42° polarizations, respectively.[77] Image (i) highlights the meta-atom shape and the polarization (red arrows), while (ii), (iii), and (iv) are PEEM images below, at, and above the E_{ph} (2.71, 2.76, and 2.78 eV, respectively) of the resonance peak. These E_{ph} are marked by the colored shapes in Figure 4c,d, which show the photoemission intensity spectra (black curves, same spectra shown in Figure 3b) and provide a visual reference for the E_{ph} location on the spectra. Images (a) and (b)(ii) show intensity concentrated within the meta-atom at low E_{ph} (red square, 2.71 eV), whereas (a) and (b)(iv) show intensity concentrated outside the meta-atom at high E_{ph} (blue triangle, 2.78 eV). At the resonance peak (black circle, 2.76 eV, images (a) and (b)(iii)), intensity is approximately equal between the interior and exterior of the meta-atom.

The switching of intensity from the interior to the exterior is the result of the overlap between the two resonances around $E_{ph} = 2.76$ eV. The lower energy resonance, whose electric field intensity resides mostly within the meta-atom interior (images (a) and (b)(ii)), is a FP type resonance.[78] The FP resonance arises from the reflection and interference of light from the top and bottom faces of the meta-atom and is unrelated to the periodic lattice of the metasurface. In contrast, the higher energy resonance (images (a) and (b)(iv)), whose electric field intensity resides mostly outside the meta-atom, is characterized by a Fano resonance that arises in dielectric metasurfaces that support Mie-type photonic modes.[79] This resonance appears in photonic band structure calculations of the metasurface as a cluster of Mie-type electric dipole (ED) modes and is typical for a metasurface or a photonic crystal with a square lattice.[5,80,81] Detailed explanation of the modes contributing to each resonance and their spatial profiles is provided in the "Mode Identification" section in Supporting Information. Although these FP and Fano resonances result in the seemingly simple field enhancement peak feature in Figure 3, the PEEM images clearly distinguish the characteristic field distribution and symmetry of the resonances involved.

To better understand how the photoemission intensity distribution in PEEM images corresponds to the electric field distribution within the meta-atom, we compare the PEEM images with the simulated counterparts. As described earlier, we reiterate that the simulations are performed via the FDTD method that compute the spatial $|\boldsymbol{E}|^4$ distribution integrated in height (weighted by IMFP) to be analogous to 2PPE-PEEM images. The simulated $|\boldsymbol{E}|^4$ maps are presented alongside the PEEM images in Figure 4a,b. Images (v), (vi), and (vii) are the simulated $|\boldsymbol{E}|^4$ images below, at, and above the (simulated) resonant E_{ph} (2.76, 2.81, and 2.83 eV, respectively). The displayed E_{ph} of the simulated images in Figure 4 have been shifted to lower E_{ph} by ≈0.05 eV (8 nm in wavelength) to line up with the PEEM images. We attribute this discrepancy to inaccuracy in modeling the exact geometry and refractive index of the metasurface. From this point forward, all E_{ph} reported for simulated results are shifted for ease of comparison.

For each simulated image in Figure 4a,b, the $|\boldsymbol{E}|^4$ distributions are similar to the photoemission intensity of the corresponding PEEM images ((ii), (iii), and (iv)). The simulations show the electric field concentrated within the meta-atom at low E_{ph} (image (v)), distributed outside the meta-atom at high E_{ph} (image (vii)), and switching at resonance (image (vi)). We note a discrepancy between PEEM and simulated image intensity at the corners of the unit cell for 42° polarization at 2.78 eV: the PEEM image in Figure 4b(iv) shows low intensity at the corners, while the same corners in the simulated image in Figure 4b(vii) show high intensity. The corner intensity does occur in the PEEM measurements but at higher E_{ph} (>2.78 eV) than shown in Figure 4 (full set of PEEM images is available in Movies, Supporting Information). As with the overall 0.05 eV shift of the simulations, the discrepancy involving the

© 2025 The Author(s). Advanced Photonics Research published by Wiley-VCH GmbH

26999293, 2025, 6, Downloaded from https://advanced.onlinelibrary.wiley.com/doi/10.1002/adpr.202400223 by Sandia National Laboratory, Wiley Online Library on [12/06/2025]. See the Terms and Conditions (https://onlinelibrary.wiley.com/terms-and-conditions) on Wiley Online Library for rules of use; OA articles are governed by the applicable Creative Commons License

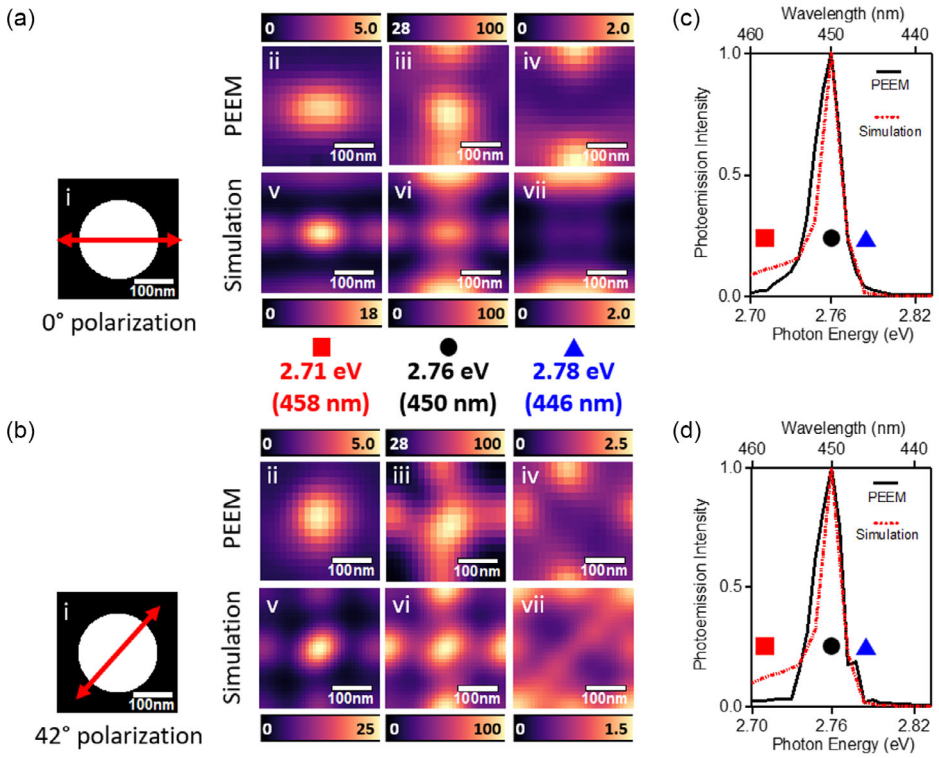


Figure 4. The PEEM photoemission intensity images of one unit cell of the metasurface are compared with the corresponding simulated $|\boldsymbol{E}|^4$ images for a) 0° and b) 42° polarizations. Pixel values in each image were chosen to optimize image contrast for ease of viewing (see numbers on scale bars). In both (a) and (b), image (i) displays the unit cell diagram where the white circle is the meta-atom and the black region is the exterior, and polarization is represented by the red arrow. Images (ii), (iii), and (iv) are the PEEM images at 2.71, 2.76, and 2.78 eV, respectively, while images (v), (vi), and (vii) are the simulated $|\boldsymbol{E}|^4$ images at 2.76, 2.81, and 2.83 eV, respectively (shifted to lower photon energy by ≈0.05 eV (8 nm) to line up with PEEM images). c) and d) plot the simulated $|\boldsymbol{E}|^4$ spectra alongside the corresponding PEEM spectra (from Figure 3b) as a function of photon energy for 0° and 42° polarizations, respectively. The colored shapes in (c) and (d) mark the photon energies for which the PEEM and simulated images in (a) and (b) are displayed. The 90° and 135° comparisons are available in Figure S3, Supporting Information.

corner intensity is attributed to imprecision in modeling. In total, the simulations reproduce the features found in the PEEM images including the switching between the two resonances, thereby showing that the photoemission intensity measured by PEEM directly corresponds to the $|\boldsymbol{E}|^4$ strength. For comparisons of all four polarizations, see Figure S3, Supporting Information.

The MEEP simulation provides spectroscopic information in addition to the spatial intensity distribution. The simulated spectra in Figure 4c,d show good agreement with those of PEEM acquired at 0° and 42° polarizations, respectively. The MEEP spectra are represented by the red curves alongside the corresponding PEEM spectra (black curves). MEEP replicates spectral features including the peak width at 2.76 eV and the asymmetric peak shape of the Fano resonances as the Mie-type modes couple to the FP resonance[78,82] on the lower E_{ph} side (left of peak). We note that the FP resonance is weaker in the PEEM spectra likely caused by imperfections in the top and bottom faces of the meta-atoms, so the PEEM intensity is lower than the simulated intensity at lower E_{ph}. Nevertheless, this result further emphasizes the switching of the photoelectron intensity between the exterior and interior of the meta-atoms at the resonance shown in both PEEM measurement and the MEEP calculations.

2.3. Impact of *k*-Vector on the PEEM Intensity Profiles

Because nonlocal metasurfaces mostly rely on the collective responses of the meta-atoms and are therefore discussed in the context of the symmetries of the meta-atoms, there is generally less emphasis on the symmetry of illumination configuration. Combination of the far-field illumination and nanoscale spatial resolution enables us to examine the local field enhancement while accessing the illumination configuration and how it can be intertwined with the polarization.

In Figure 4b, we demonstrate the effect of the incident polarization manifesting as small intensity differences between Fano resonance features for 42° between E_{ph} of 2.76 eV and 2.78 eV (black circle, images (iii) and (vi), and blue triangle, images (iv) and (vii), respectively). We visualize in greater detail the evolution of the field patterns between 2.76 and 2.78 eV in smaller E_{ph} increments for the two diagonal polarizations of a) 42° and b) 135°, as shown in **Figure 5**. Images (ii) through (vi) are the PEEM images, and images (vii) through (xi) are the corresponding simulated images. Since 45° and 135° polarizations should be an equal mix of the 0° and 90° polarizations, the PEEM images under 45° and 135° polarizations should exhibit features of both 0° and 90° polarization images in equal proportion. The Fano

© 2025 The Author(s). Advanced Photonics Research published by Wiley-VCH GmbH

26999293, 2025, 6, Downloaded from https://advanced.onlinelibrary.wiley.com/doi/10.1002/adpr.202400223 by Sandia National Laboratory, Wiley Online Library on [12/06/2025]. See the Terms and Conditions (https://onlinelibrary.wiley.com/terms-and-conditions) on Wiley Online Library for rules of use; OA articles are governed by the applicable Creative Commons License

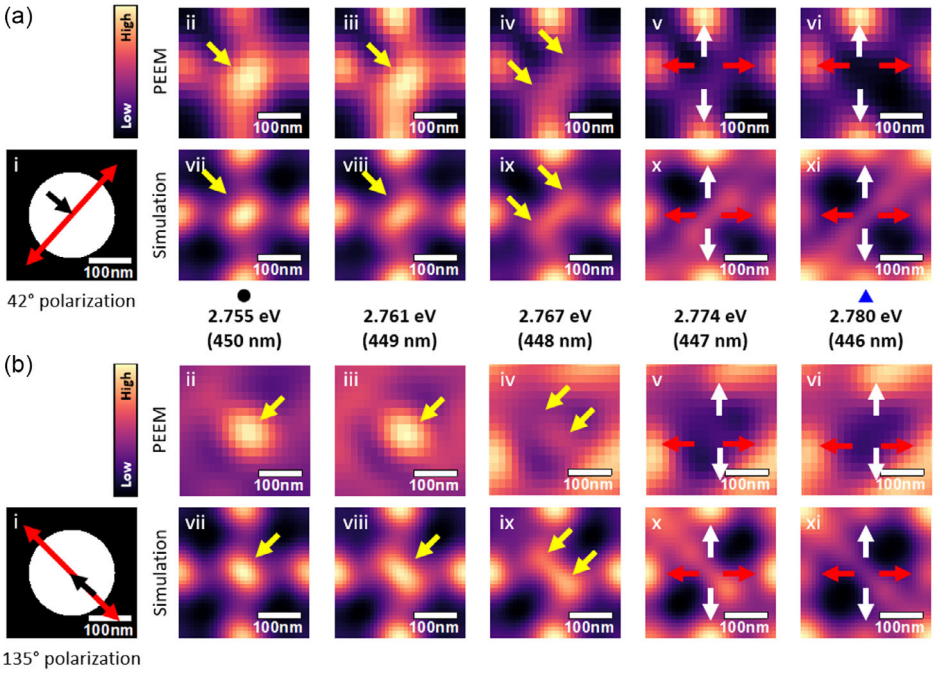


Figure 5. Comparison of the evolution of the field patterns between PEEM data and simulations for a) 42° polarization and b) 135° polarization. Image (i) displays the unit cell diagram with polarization represented by the red arrow. The black arrows in (i) show the propagation direction of the excitation light source within the *x*–*y* plane ($k_{||}$) due to the slight tilt of the incoming light from the surface normal. Images (ii) through (vi) are the PEEM images between 2.755 eV (black circle) and 2.780 eV (blue triangle) while images (vii) through (xi) are the simulated $|\boldsymbol{E}|^4$ images for the corresponding E_{ph} (rounded to three decimal places due to smaller E_{ph} increments). The colored shapes (black circle, blue triangle) correspond to the two E_{ph} displayed in Figure 4. The white and red arrows in (v), (vi), (x), and (xi) for both (a) and (b) point to Fano resonance features from 0° and 90° polarizations, respectively. The yellow arrows in (ii) and (iv) for both (a) and (b) mark the elongation of the intensity near the center. Color scale for each image was adjusted to prioritize ease of viewing of the field patterns and differs slightly in contrast from images in Figure 4.

features (exterior of meta-atom) in PEEM images for 42° polarization are marked by the white and red arrows respectively in Figure 5a(v,vi). Most importantly, the features highlighted by the white arrows have higher intensity than the features highlighted by the red arrows. The unequal intensities between the highlighted features originate from the polarization being at 42°, rather than exactly at 45°. The MEEP image modeled using 42° polarization reproduces the same inequality as highlighted by the white and red arrows in Figure 5a(x,xi), confirming that the intensity inequality is an effect of the polarization. In contrast, we expect the features highlighted by the arrows in Figure 5b (135° polarization) to exhibit equal contributions, which is what we observed. The features marked by the white and red arrows in images (v) and (vi) have similar intensities, and the simulated images (x) and (xi) reproduce the same effect. We note that small deviations from 0° (90°) cannot be detected, as the 90° (0°) component becomes very small (≈5% for 3° deviation) and further reduced by the 2PPE dependence on $|\boldsymbol{E}|^4$. Altogether, PEEM measures the effect of slight deviations from the nominal polarization angle that appears more effectively near 45° or 135° polarizations.

Further examination of the 42° and 135° polarizations in Figure 5 reveals the subtle impact of small deviations of the illuminating light from the surface normal. The deviation is described by the polar angle θ and azimuthal angle φ (defined in Figure 1c) and determines the direction of the surface parallel component $k_{||}$ of the incident *k*-vector. The presence of $k_{||}$ affects the symmetry of the switching of the electric field intensity between the meta-atom interior and exterior. In the PEEM images and the simulated electric field images for 0° and 90° polarizations (Figure S3a,c, Supporting Information respectively), the field patterns are simply 90° rotations of each other, which is expected due to the 90° rotational symmetry of the metasurface. On the other hand, the PEEM images for 42° polarization shown in Figure 5a do not replicate those of 135° polarization in Figure 5b by 90° rotation. For 42° polarization (Figure 5a(ii–iv)), the yellow arrows point to the intensity at the center of the PEEM image as it elongates toward higher E_{ph}. In (iv), the yellow arrows point to the two sides of the elongated central intensity, which are approximately equal in brightness. The simulations replicate the elongation using a polar angle θ of 0.1° and azimuthal angle φ of 130° ($k_{||}$ is represented by the black arrow in Figure 5a(i). See Table S1, Supporting Information, for the simulated polar and azimuthal angles at each polarization.). In the simulated images in Figure 5a(vii–ix), the central intensity (highlighted by yellow arrows) elongates with the same intensity on both ends. The even elongation occurs because $k_{||}$ is nearly perpendicular to the 42° polarization direction, leaving the polarization vector nearly unchanged from illumination tilt by θ. In contrast, for 135°

© 2025 The Author(s). Advanced Photonics Research published by Wiley-VCH GmbH

26999293, 2025, 6, Downloaded from https://advanced.onlinelibrary.wiley.com/doi/10.1002/adpr.202400223 by Sandia National Laboratory, Wiley Online Library on [12/06/2025]. See the Terms and Conditions (https://onlinelibrary.wiley.com/terms-and-conditions) on Wiley Online Library for rules of use; OA articles are governed by the applicable Creative Commons License

26999293, 2025, 6, Downloaded from https://advanced.onlinelibrary.wiley.com/doi/10.1002/adpr.202400223 by Sandia National Laboratory, Wiley Online Library on [12/06/2025]. See the Terms and Conditions (https://onlinelibrary.wiley.com/terms-and-conditions) on Wiley Online Library for rules of use; OA articles are governed by the applicable Creative Commons License

polarization (Figure 5b(ii–iv)), the elongation highlighted by yellow arrows does not occur evenly, that is, one end of the elongation in (iv) is dimmer than the other. The corresponding simulation replicates the uneven elongation as shown in Figure 5b(vii–ix), using $\theta = 0.15°$ and $\varphi = 310°$ ($k_{\parallel}$ is represented by the black arrow in Figure 5b(i)). In this case, $k_{\parallel}$ is nearly parallel to the polarization vector, introducing a component of polarization (E-field) perpendicular to the surface (z-axis). The resulting field has an odd symmetry with respect to 180° rotation about the z-axis and causes uneven elongation,[83] as opposed to the even symmetry of the 42° case where the elongation is close to even. Overall, the metasurface is sensitive to the minute (≈0.1°) variations in the incident light configuration manifested by the additional $k_{\parallel}$ component.[35] This subtle effect resulting from the intertwined illumination configuration and polarization is correctly reflected in the measured PEEM intensity distribution, revealing the impact of the incident k-vector.

2.4. Estimation of Electron Inelastic Mean Free Path

To estimate the electron IMFP, we leverage the shifting of the electromagnetic field intensities of the two resonances between the meta-atom interior and the exterior (as defined in Figure 2a). Since each region has a different TiO_2 thickness, the photoemission intensity from each region is attenuated differently. Therefore, comparing the total interior intensity (I_{int}) to the total exterior intensity (I_{ext}), defined as the sum of intensity across all points within the region (interior or exterior), is suitable for determining the IMFP. To quantitatively compare the intensities, we use the ratio of I_{int} to I_{ext}, that is, (I_{int}/I_{ext}). We explain in the following how the different TiO_2 thicknesses affect the photoemission intensity from the regions.

The attenuation of photoelectrons from the interior and exterior is impacted by the SiO_2 substrate as well as the IMFP. Because the exterior TiO_2 layer is thin (≈10 nm) compared to the TiO_2 meta-atom itself (≈75 nm), the exterior photoemission should be influenced by the SiO_2 substrate underneath. However, since SiO_2 has a much lower PEY than TiO_2 as shown in Figure S2, Supporting Information, photoemission from the SiO_2 substrate is negligible, leaving the exterior TiO_2 layer as the only significant photoemitting source from the exterior area. The simulation accounts for this PEY difference during the integration of the x–y image slices. Given that the exterior TiO_2 is thin, photoemission from this region (I_{ext}) is not significantly attenuated for IMFP on the length scale of 10s of nm. In contrast, I_{int} is influenced almost entirely by the *meta*-atom itself, which is ≈8 times the thickness of the exterior TiO_2 layer. Photoelectrons from within the meta-atom are significantly attenuated if emitted at depths greater than or equal to the IMFP, so the IMFP affects how much of the meta-atom volume is sampled via PEEM. Because of the different sensitivity of the two TiO_2 thicknesses on IMFP, the ratio of the intensity from the two regions (I_{int}/I_{ext}) is a quantifiable measure to examine the impact of IMFP on the PEEM and simulated images. We note that the choice of comparing the intensities in the interior and exterior is further corroborated by the singular value decomposition of the PEEM and simulated images as described in the "Details on IMFP Extraction" section in Supporting Information.

To find the IMFP, we vary the IMFP in simulations and match the simulated intensity ratio (I_{int}/I_{ext}) as a function of E_{ph} to those calculated from PEEM images. We compare the ratios in **Figure 6**, where the PEEM data are represented by the circle, square, cross, and triangle markers for 0°, 42°, 90°, and 135° polarizations, respectively. The solid, black curve is the simulated (0° polarization) intensity ratio for an IMFP value of 35 nm, and the shaded region bounded by the dotted and dashed curves covers a range of intensity ratios for IMFP values from 25 to 45 nm. The simulated intensity ratios match well with the PEEM intensity ratios between E_{ph} of 2.76 and 2.82 eV. Below 2.76 eV, the simulated intensity ratio shows some deviation, exhibiting a dip around 2.75 eV. This discrepancy is due to the difference in the simulated spectra in Figure 4c,d, where the low-energy tail of the simulated spectra is higher than that of PEEM. The Fano resonance (intensity outside the meta-atom) does not "turn on" in PEEM images as strongly as in the simulations as E_{ph} is increased, resulting in a more exterior contribution to the intensity ratio in the simulations. The simulated image in Figure 4a(v)

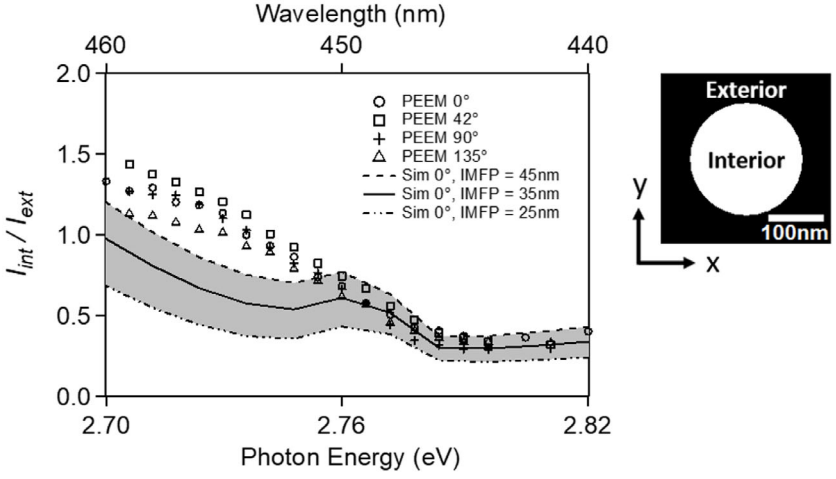


Figure 6. Ratio of the intensity inside the meta-atom to the exterior intensity, I_{int}/I_{ext}, plotted as a function of photon energy, comparing between experimental data (all polarizations) and simulation (0° polarization) for electron IMFP of 35 nm (shaded region covers IMFP variation of ±10 nm).

© 2025 The Author(s). Advanced Photonics Research published by Wiley-VCH GmbH

26999293, 2025, 6, Downloaded from https://advanced.onlinelibrary.wiley.com/doi/10.1002/adpr.202400223 by Sandia National Laboratory, Wiley Online Library on [12/06/2025]. See the Terms and Conditions (https://onlinelibrary.wiley.com/terms-and-conditions) on Wiley Online Library for rules of use; OA articles are governed by the applicable Creative Commons License

corroborates this behavior, exhibiting some intensity outside the meta-atom while the PEEM image in Figure 4a(ii) shows intensity only near the center. In the present analysis, we assume that the electron IMFP is constant across the narrow range of E_{ph} in Figure 6. Because the literature values of the electron IMFP tend to have wider variation closer to zero kinetic energy, we placed greater emphasis on fitting the simulated intensity ratio at E_{ph} of 2.76 eV and above.

Based on the intensity ratio between the interior and exterior of the meta-atom, we determine the best-fit electron IMFP value to be 35 ± 10 nm. This IMFP is larger than reported values of IMFP in metals for electrons of similar kinetic energy (3–10 nm)[57–63] but is closer to the reported calculated values of dielectric materials (10–100 nm).[64–66] The IMFP is comparable in magnitude to the height of the meta-atoms (≈75 nm), confirming that the intensity distribution in the PEEM images includes significant contributions from electromagnetic fields within the meta-atom volume. We anticipate that this IMFP can be applied to analyze PEEM images of metasurfaces made of other dielectric materials when the IMFP is not known a priori, as IMFP is mostly universal among materials with similar electronic properties (i.e., dielectric material category). We admit that analyzing PEEM images of nanophotonic systems of different dielectric materials using this IMFP would include inaccuracy, which should be alleviated by expanding data of the IMFP across various materials at the very low electron kinetic energy range. For nanostructures much taller than the IMFP, we expect that our PEEM approach evaluates the electric fields only within the upper part of the structures. Nonetheless, the long electron IMFP within dielectric materials validates the PEEM visualization of the field distribution of photonic resonances within the volume of dielectric nanophotonic structures.

3. Conclusion

In this study, we have demonstrated subwavelength resolution imaging of volume-type photonic resonances within dielectric nanostructures using PEEM. We imaged the resonances within a TiO_2 metasurface as the polarization and photon energy (E_{ph}) are varied in the visible range using a two-photon photoemission process. The metasurface was designed to support two resonances (FP and Fano) that overlap in E_{ph} and shift their field intensity between areas of different TiO_2 thicknesses as E_{ph} is changed. To understand the PEEM images, we simulated the images via finite-difference time-domain method that integrates the intensity in height weighted by the electron IMFP. By leveraging the shift in intensity between the two overlapping resonances, we determined this IMFP of very low kinetic energy (<1 eV) photoelectrons to be 35 ± 10 nm. Using an iterative approach to optimize the spatial intensity distribution of the images with the IMFP, the simulated images matched well with PEEM images as a function of E_{ph} and polarization. The simulated images also reproduced the subtle effects on the metasurface caused by deviation of the excitation light (*k*-vector) from normal incidence, showing that PEEM can image such effects. The agreement between the simulations and PEEM images, along with the long IMFP that is comparable to the feature size of the meta-atoms, establishes that PEEM measures the electromagnetic field distribution within the volume of the nanostructures. The IMFP also corroborates experimentally the calculations suggesting dielectric materials generally have higher IMFP (10–100 nm) than metals (3–10 nm) at this low kinetic energy range. All told, our work showcases the detailed characterization of dielectric metasurfaces using PEEM as an avenue for studying localized field enhancement in dielectric nanophotonic systems attained via far-field illumination.

4. Experimental Section

Sample Fabrication: We fabricated all metasurfaces on JGS2-grade fused silica substrates. TiO_2 films were deposited using ALD (Picosun) via a thermal process at 150 °C, with alternating cycles of $TiCl_4$ (0.1 s dose, 6 s purge) and water (0.2 s dose, 8 s purge). Following deposition, soft masks were generated using electron beam lithography (JEOL) with ZEP520A. The exposed samples were developed in n-amyl acetate for 90 s. After development, the soft mask profile was transferred into the TiO_2 layer using a reactive ion etching (Plasma-Therm) process at 30 mT with CF_4 (42 sccm) and O_2 (10 sccm), maintaining a platen temperature of 20 °C, 75 W RF power, and 800 W inductively coupled plasma (ICP) power. Excess resist was removed using N-methyl-2-pyrrolidone at 80 °C. After etching, the samples were coated with an additional 10 nm of TiO_2 via ALD to serve as a thin charge dissipation layer.

The TiO_2 thin films used to calibrate the photoemission yield were grown using a different ALD system. The thin films were grown in a Cambridge NanoTech Savannah S100 reactor using tetrakis(dimethylamido)titanium(IV) (TDMAT, Strem Chemicals) and deionized water (18.5 megohm). The precursors were contained in stainless-steel ampoules maintained at 75 °C (TDMAT) and 22 °C (H_2O), respectively, and were delivered by direct-draw at the pressure of the reactor (base pressure: 90 mTorr, process pressure 300–350 mTorr). Ultrahigh purity argon (99.999%, Matheson) was used as the carrier and purge gas (20 sccm). Samples were subjected to 10 min of UV ozone exposure prior to loading into the ALD reactor to remove surface hydrocarbons. TiO_2 films were grown at 150 °C using the recipe:[84,85] H_2O pulse (0.05 s), purge (30 s), TDMAT pulse (0.25 s), and purge (30 s). The ALD cycle was repeated a plurality of times to afford the desired film thickness. Si(100) monitor coupons (University Wafer) were included during each ALD experiment. TiO_2 films grown on the Si(100) coupons were measured using a Woollam RC2 spectroscopic ellipsometer (Cauchy model) to determine the film thickness and confirm a consistent growth rate of 0.47 ± 0.01 Å cycle^{-1}.

Linear Measurements: We measured the linear spectra of the metasurface using a homebuilt system. Before the far-field reflectivity and transmissivity measurements were acquired, the sample was cleaned by annealing at ≈150 °C in UHV conditions to remove water and other physisorpted chemical species from prolonged exposure to air. A polarized broadband white light emission from a thermal source (Tungsten-Halogen Light Source) was focused onto the sample using an achromatic lens of 25 mm focal length. The reflected or transmitted light was then routed toward the entrance slit of a spectrometer (Maya2000 pro, Ocean Optics). The low numerical aperture (0.1) of the imaging system limits the excitation angle of incident light, which preserves the quality factor of the optical modes. Because the spectrometer used in this system is different from the one used during PEEM measurements, we calibrated the two spectrometers against each other and against absolute calibration data using Xe calibration lamps (Oriel Instruments).

PEEM Imaging: We conducted near-field imaging using a LEEM-III system (Elmitec Elektronenmikroskopie GmbH), operated as a photoelectron emission microscope (PEEM). The PEEM instrument is connected to the output of a tunable near-infrared (IR) Ti:Sapphire laser oscillator (normal incident, ≈100 femtosecond pulse, Coherent Inc.) and a Harmonixx second harmonic generation (SHG) system (A.P.E.) for doubling the frequency of the Ti:Sapphire laser. The spectral width of the Ti:Sapphire laser is ≈0.5–1% of the wavelength with some variations depending on the

 © 2025 The Author(s). Advanced Photonics Research published by Wiley-VCH GmbH

exact wavelength. The SHG output was focused onto the sample surface (spot sizes of ≈100 μm) using a fused silica lens of 750 mm focal length. The polarizations of the lasers were rotated with half waveplates. In addition, a deep UV laser (normal incident, 213 nm continuous wave, Toptica Photonics) and incoherent, deep UV–vis light source (incident angle of 73° relative to the sample surface normal, continuous wave, Energetiq Technology) with a Czerny–Turner monochromator (Acton Research Corporation) were used for sample navigation while the main data was collected using SHG.

Prior to PEEM measurement, we loaded the metasurface inside the PEEM instrument in an ultrahigh vacuum (base pressure 3×10^{-11} Torr in LEEM-III system) and annealed it overnight at ≈150 °C to remove water and other chemical species physisorbed from the air. During data acquisition, pressure did not exceed 1×10^{-10} Torr, and sample temperature did not exceed 50 °C (small amount of heating due to light source).

Details on PEEM data processing are available in the Supporting Information.

Supporting Information

Supporting Information is available from the Wiley Online Library or from the author.

Acknowledgements

The authors thank P. Mantos for his measurement support. A.R.K., C.F.D., J.Y., I.B., R.S., A.C., and T.O. acknowledge support from the US Department of Energy, Office of Science, Division of Materials Sciences and Engineering (grant BES 20-017574). F.J.V., A.M.B., and J.P.K. acknowledge support from the Laboratory Directed Research and Development program at Sandia National Laboratories. Work was performed, in part, at the Center for Integrated Nanotechnologies, an Office of Science User Facility operated for the US Department of Energy, Office of Science. Sandia National Laboratories is a multimission laboratory managed and operated by National Technology and Engineering Solutions of Sandia, LLC., a wholly owned subsidiary of Honeywell International, Inc., for the US Department of Energy's National Nuclear Security Administration under contract DE-NA0003525. This article describes objective technical results and analysis. Any subjective views or opinions that might be expressed in the article do not necessarily represent the views of the US Department of Energy or the United States Government.

Conflict of Interest

The authors declare no conflict of interest.

Author Contributions

Andrew R. Kim: data curation (lead); formal analysis (lead); investigation (equal); methodology (lead); software (lead); visualization (lead); writing—original draft (lead); writing—review and editing (lead). **Chloe F. Doiron**: resources (lead); writing—original draft (supporting). **Fernando J. Vega**: investigation (equal). **Jaeyeon Yu**: investigation (supporting); writing—review and editing (supporting). **Alex M. Boehm**: formal analysis (supporting); investigation (supporting); methodology (supporting); writing—review and editing (supporting). **Joseph P. Klesko**: resources (supporting); writing—original draft (supporting); writing—review and editing (supporting). **Igal Brener**: formal analysis (supporting); project administration (lead); visualization (supporting); writing—review and editing (supporting). **Raktim Sarma**: formal analysis (supporting); investigation (supporting); visualization (supporting); writing—review and editing (supporting). **Alexander Cerjan**: formal analysis (supporting); software (supporting); visualization (supporting); writing—original draft (supporting); writing—review and editing (supporting). **Taisuke Ohta**: conceptualization (lead); formal analysis (supporting); funding acquisition (supporting); investigation (supporting); methodology (supporting); supervision (lead); visualization (supporting); writing—original draft (supporting); writing—review and editing (supporting).

Data Availability Statement

The data that support the findings of this study are available from the corresponding author upon reasonable request.

Keywords

electron inelastic mean free path, metasurfaces, nanophotonics, near-field imaging, near-field spectroscopy, photoelectron emission microscopy

Received: February 9, 2025
Published online: March 21, 2025

[1] C. L. Holloway, E. F. Kuester, J. A. Gordon, J. O'Hara, J. Booth, D. R. Smith, *IEEE Antennas Propag. Mag.* **2012**, *54*, 10.
[2] N. Yu, P. Genevet, M. A. Kats, F. Aieta, J.-P. Tetienne, F. Capasso, Z. Gaburro, *Science* **2011**, *334*, 333.
[3] I. Brener, S. Liu, I. Staude, J. Valentine, C. Holloway, in *Dielectric Metamaterials: Fundamentals, Designs and Applications*, Woodhead Publishing, Cambridge, MA **2019**.
[4] S. A. Schulz, R. F. Oulton, M. Kenney, A. Alù, I. Staude, A. Bashiri, Z. Fedorova, R. Kolkowski, A. F. Koenderink, X. Xiao, J. Yang, W. J. Peveler, A. W. Clark, G. Perrakis, A. C. Tasolamprou, M. Kafesaki, A. Zaleska, W. Dickson, D. Richards, A. Zayats, H. Ren, Y. Kivshar, S. Maier, X. Chen, M. A. Ansari, Y. Gan, A. Alexeev, T. F. Krauss, A. Di Falco, S. D. Gennaro, et al., *Appl. Phys. Lett.* **2024**, *124*, 260701.
[5] J. D. Joannopoulos, S. G. Johnson, J. N. Winn, R. D. Meade, in *Photonic Crystals: Molding The Flow of Light*, 2nd ed., Princeton University Press, Princeton, NJ **2008**.
[6] R. K. Cersonsky, J. Antonaglia, B. D. Dice, S. C. Glotzer, *Nat. Commun.* **2021**, *12*, 2543.
[7] X. Chen, Y. Zhang, G. Cai, J. Zhuo, K. Lai, L. Ye, *Nanophotonics* **2022**, *11*, 4537.
[8] K. Wang, H. Liu, Z. Li, M. Liu, Y. Zhang, H. Zhang, *Results Phys.* **2023**, *46*, 106276.
[9] D. Lee, J. Gwak, T. Badloe, S. Palomba, J. Rho, *Nanoscale Adv.* **2020**, *2*, 605.
[10] C. Schlickriede, S. S. Kruk, L. Wang, B. Sain, Y. Kivshar, T. Zentgraf, *Nano Lett.* **2020**, *20*, 4370.
[11] J. Engelberg, C. Zhou, N. Mazurski, J. Bar-David, A. Kristensen, U. Levy, *Nanophotonics* **2020**, *9*, 361.
[12] M. Gopakumar, G.-Y. Lee, S. Choi, B. Chao, Y. Peng, J. Kim, G. Wetzstein, *Nature* **2024**, *629*, 791.
[13] P. Genevet, F. Capasso, *Rep. Prog. Phys.* **2015**, *78*, 024401.
[14] K. E. Chong, L. Wang, I. Staude, A. R. James, J. Dominguez, S. Liu, G. S. Subramania, M. Decker, D. N. Neshev, I. Brener, Y. S. Kivshar, *ACS Photonics* **2016**, *3*, 514.
[15] M. Khorasaninejad, W. T. Chen, R. C. Devlin, J. Oh, A. Y. Zhu, F. Capasso, *Science* **2016**, *352*, 1190.
[16] W. T. Chen, A. Y. Zhu, V. Sanjeev, M. Khorasaninejad, Z. Shi, E. Lee, F. Capasso, *Nat. Nanotechnol.* **2018**, *13*, 220.
[17] A. Krasnok, M. Tymchenko, A. Alu, *Mater. Today* **2018**, *21*, 8.

© 2025 The Author(s). Advanced Photonics Research published by Wiley-VCH GmbH

26999293, 2025, 6, Downloaded from https://advanced.onlinelibrary.wiley.com/doi/10.1002/adpr.202400223 by Sandia National Laboratory, Wiley Online Library on [12/06/2025]. See the Terms and Conditions (https://onlinelibrary.wiley.com/terms-and-conditions) on Wiley Online Library for rules of use; OA articles are governed by the applicable Creative Commons License

[18] R. Camacho-Morales, M. Rahmani, S. Kruk, L. Wang, L. Xu, D. A. Smirnova, A. S. Solntsev, A. Miroshnichenko, H. H. Tan, F. Karouta, S. Naureen, K. Vora, L. Carletti, C. de Angelis, C. Jagadish, Y. S. Kivshar, D. N. Neshev, *Nano Lett.* **2016**, *16*, 7191.
[19] C. F. Doiron, J. B. Khurgin, G. V. Naik, *Adv. Opt. Mater.* **2022**, *10*, 2201084.
[20] R. C. Devlin, M. Khorasaninejad, W. T. Chen, J. Oh, F. Capasso, *Proc. Natl. Acad. Sci. U.S.A* **2016**, *113*, 10473.
[21] M. Khorasaninejad, W. T. Chen, A. Y. Zhu, J. Oh, R. C. Devlin, C. Roques-Carmes, I. Mishra, F. Capasso, *IEEE J. Sel. Top. Quantum Electron.* **2017**, *23*, 4700216.
[22] Y. Cai, Y. Huang, K. Zhu, H. Wu, *Opt. Lett.* **2021**, *46*, 4049.
[23] K. Koshelev, S. Lepeshov, M. Liu, A. Bogdanov, Y. Kivshar, *Phys. Rev. Lett.* **2018**, *121*, 193903.
[24] A. C. Overvig, S. C. Malek, M. J. Carter, S. Shrestha, N. Yu, *Phys. Rev. B* **2020**, *102*, 035434.
[25] A. F. Doiron, I. Brener, A. Cerjan, *Nat. Commun.* **2022**, *13*, 7534.
[26] S. Campione, S. Liu, L. I. Basilio, L. K. Warne, W. L. Langston, T. S. Luk, J. R. Wendt, J. L. Reno, G. A. Keeler, I. Brener, M. B. Sinclair, *ACS Photonics* **2016**, *3*, 2362.
[27] G. Q. Moretti, A. Tittl, E. Cortés, S. A. Maier, A. V. Bragas, G. Grinblat, *Adv. Photonics Res.* **2022**, *2*, 2200111.
[28] J. P. S. Fitzgerald, R. C. Word, S. D. Saliba, R. Könenkamp, *Phys. Rev. B* **2013**, *87*, 205419.
[29] A. Boehm, S. D. Gennaro, C. F. Doiron, T. E. Beechem, M. B. Sinclair, I. Brener, R. Sarma, T. Ohta, *APL Photonics* **2024**, *9*, 066103.
[30] J. Cheng, S. Inampudi, H. Mosallaei, *Sci. Rep.* **2017**, *7*, 12228.
[31] N. Kim, M. Kim, J. Jung, T. Chang, S. Jeon, J. Shin, *Nanophotonics* **2023**, *12*, 2347.
[32] J. Wu, F. Tang, J. Ma, Q. Li, S. Shang, J. Chen, Y. Wu, Y. Wang, X. Ye, W. Zheng, R. Zhu, *Results Phys.* **2020**, *18*, 103226.
[33] H. Yu, Q. Sun, K. Ueno, T. Oshikiri, A. Kubo, Y. Matsuo, H. Misawa, *ACS Nano* **2016**, *10*, 10373.
[34] A. Neff, F. Niefind, B. Abel, S. C. B. Mannsfeld, K. R. Siefermann, *Adv. Mater.* **2017**, *29*, 1701012.
[35] P. P. Joshi, R. Li, J. L. Spellberg, L. Liang, S. B. King, *Nano Lett.* **2022**, *22*, 3180.
[36] K. Stallberg, G. Lilienkamp, W. Daum, *J. Phys. Chem. C* **2017**, *121*, 13833.
[37] E. Bauer, in *Surface Microscopy With Low Energy Electrons*, Springer, New York, NY **2014**.
[38] S. Mignuzzi, M. Mota, T. Coenen, Y. Li, A. P. Mihai, P. K. Petrov, R. F. M. Oulton, S. A. Maier, R. Sapienza, *ACS Photonics* **2018**, *5*, 1381.
[39] T. Coenen, J. van de Groep, A. Polman, *ACS Nano* **2013**, *7*, 1689.
[40] A. Polman, M. Kociak, F. J. García de Abajo, *Nat. Mater.* **2019**, *18*, 1158.
[41] F. Yang, P. A. Huidobro, J. B. Pendry, *Laser Photonics Rev.* **2020**, *14*, 2000055.
[42] L. Yin, V. K. Vlasko-Vlasov, A. Rydh, J. Pearson, U. Welp, S.-H. Chang, S. K. Gray, G. C. Schatz, D. B. Brown, C. W. Kimball, *Appl. Phys. Lett.* **2004**, *85*, 467.
[43] B. J. Bohn, M. Schnell, M. A. Kats, F. Aieta, R. Hillenbrand, F. Capasso, *Nano Lett.* **2015**, *15*, 3657.
[44] T. J. Davis, D. Janoschka, P. Dreher, B. Frank, *Science* **2020**, *368*, eaba6415.
[45] G. Spektor, D. Kilbane, A. K. Mahro, B. Frank, S. Ristok, L. Gal, D. Podbiel, S. Mathias, H. Giessen, *Science* **2017**, *355*, 1187.
[46] P. Kahl, S. Wall, C. Witt, C. Schneider, D. Bayer, A. Fischer, P. Melchior, M. Horn-von Hoegen, M. Aeschlimann, *Plasmonics* **2014**, *9*, 1401.
[47] M. Dąbrowski, Y. Dai, A. Argondizzo, Q. Zou, X. Cui, H. Petek, *ACS Photonics* **2016**, *3*, 1704.
[48] A. Kubo, K. Onda, H. Petek, Z. Sun, Y. S. Jung, H. K. Kim, *Nano Lett.* **2005**, *5*, 1123.
[49] M. Cinchetti, A. Gloskovskii, S. A. Nepjiko, G. Schönhense, H. Rochholz, M. Kreiter, *Phys. Rev. Lett.* **2005**, *95*, 047601.
[50] B. Franks, P. Kahl, D. Podbiel, G. Spektor, M. Orenstein, L. Fu, T. Weiss, M. Horn-von Hoegen, T. J. Davis, *Sci. Adv.* **2017**, *3*, e1700721.
[51] Q. Sun, S. Zu, H. Misawa, *J. Chem. Phys.* **2020**, *153*, 120902.
[52] L. Zhang, A. Kubo, L. Wang, H. Petek, T. Seideman, *Phys. Rev. B* **2011**, *84*, 245442.
[53] Y. Gong, A. G. Joly, P. Z. El-Khoury, W. P. Hess, *J. Phys. Chem. C* **2014**, *118*, 25671.
[54] C. J. Powell, *J. Electron Spectrosc. Relat. Phenom.* **1988**, *47*, 197.
[55] M. P. Seah, W. A. Dench, *Surf. Interface Anal.* **1979**, *1*, 2.
[56] F. Boschini, M. Zonno, A. Damascelli, *Rev. Mod. Phys.* **2024**, *96*, 015003.
[57] C. D. Denton, I. Abril, R. Garcia-Molina, J. C. Moreno-Marín, S. Heredia-Avalos, *Surf. Interface Anal.* **2008**, *40*, 1481.
[58] D. R. Penn, *Phys. Rev. B* **1987**, *35*, 482.
[59] H. Shinotsuka, S. Tanuma, C. J. Powell, D. R. Penn, *Surf. Interface Anal.* **2015**, *47*, 871.
[60] H. T. Nguyen-Truong, *J. Phys. Chem. C* **2015**, *119*, 7883.
[61] H. Kanter, *Phys. Rev. B* **1970**, *1*, 522.
[62] Y. Okuda, J. Kawakita, T. Taniuchi, H. Shima, A. Shimizu, Y. Naitoh, K. Kinoshita, H. Akinaga, S. Shin, *Jpn. J. Appl. Phys.* **2020**, *59*, SGGB02.
[63] O. Y. Ridzel, V. Astašauskas, W. S. M. Werner, *J. Electron Spectrosc. Relat. Phenom.* **2020**, *241*, 146824.
[64] S. Tanuma, *Vac. Surf. Sci.* **2022**, *65*, 102.
[65] H. Shinotsuka, S. Tanuma, C. J. Powell, D. R. Penn, *Surf. Interface Anal.* **2019**, *51*, 427.
[66] M. A. Flores-Mancera, J. S. Villarrubia, *ACS Omega* **2020**, *5*, 4139.
[67] E. Antonsson, F. Gerke, B. Langer, C. Goroncy, T. Dresch, T. Leisner, C. Graf, E. Rühl, *Phys. Chem. Chem. Phys.* **2023**, *25*, 15173.
[68] M. Berg, K. Keyshar, I. Bilgin, F. Liu, H. Yamaguchi, R. Vajtai, C. Chan, G. Gupta, S. Kar, P. Ajayan, T. Ohta, A. D. Mohite, *Phys. Rev. B* **2017**, *95*, 235406.
[69] S. Hüfner, in *Photoelectron Spectroscopy - Principles and Applications*, Springer-Verlag, Berlin **2003**.
[70] F. Bisio, M. Nývlt, J. Franta, H. Petek, J. Kirschner, *Phys. Rev. Lett.* **2006**, *96*, 087601.
[71] M. Reutzel, A. Li, H. Petek, *Phys. Rev. B* **2020**, *101*, 075409.
[72] C. Dette, M. A. Pérez-Osorio, C. S. Kley, P. Punke, C. E. Patrick, P. Jacobson, F. Giustino, S. J. Jung, K. Kern, *Nano Lett.* **2014**, *14*, 6533.
[73] T. Luttrell, S. Halpegamage, J. Tao, A. Kramer, E. Sutter, M. Batzill, *Sci. Rep.* **2014**, *4*, 4043.
[74] H. Ueba, B. Gumhalter, *Prog. Surf. Sci.* **2007**, *82*, 193.
[75] N. V. Tkachenko, in *Optical Spectroscopy: Methods and Instrumentations*, Elsevier, Oxford **2006**.
[76] A. F. Oskooi, D. Roundy, M. Ibanescu, P. Bermel, J. D. Joannopoulos, S. G. Johnson, *Comput. Phys. Commun.* **2010**, *181*, 687.
[77] We chose 42° instead of 45° so that the polarization is not perfectly along a symmetry direction to visualize the effect on the symmetry of the field patterns.
[78] A. A. Bogdanov, K. L. Koshelev, P. V. Kapitanova, M. V. Rybin, S. A. Gladyshev, Z. F. Sadrieva, K. B. Samusev, Y. S. Kivshar, M. F. Limonov, *Adv. Photonics* **2019**, *1*, 016001.
[79] T. Liu, R. Xu, P. Yu, Z. Wang, J. Takahara, *Nanophotonics* **2020**, *9*, 1115.
[80] J. Lee, B. Zhen, S.-L. Chua, W. Qiu, J. D. Joannopoulos, M. Solijačić, O. Shapira, *Phys. Rev. Lett.* **2012**, *109*, 067401.

© 2025 The Author(s). Advanced Photonics Research published by Wiley-VCH GmbH

26999293, 2025, 6, Downloaded from https://advanced.onlinelibrary.wiley.com/doi/10.1002/adpr.202400223 by Sandia National Laboratory, Wiley Online Library on [12/06/2025]. See the Terms and Conditions (https://onlinelibrary.wiley.com/terms-and-conditions) on Wiley Online Library for rules of use; OA articles are governed by the applicable Creative Commons License

[81] S. Fan, *Phys. Rev. B* **2002**, *65*, 235112.
[82] M. F. Limonov, M. V. Rybin, A. N. Poddubny, Y. S. Kivshar, *Nat. Photonics* **2017**, *11*, 543.
[83] S. Moser, *J. Electron Spectrosc. Relat. Phenom.* **2017**, *214*, 29.
[84] Q. Xie, Y.-L. Jiang, C. Detavernier, D. Deduytsche, R. L. Van Meirhaeghe, G.-P. Ru, B.-Z. Li, X.-P. Qu, *J. Appl. Phys.* **2007**, *102*, 083521.
[85] R. Katamreddy, V. Omarjee, B. Feist, C. Dussarrat, *ECS Trans.* **2008**, *16*, 113.

© 2025 The Author(s). Advanced Photonics Research published by Wiley-VCH GmbH

26999293, 2025, 6, Downloaded from https://advanced.onlinelibrary.wiley.com/doi/10.1002/adpr.202400223 by Sandia National Laboratory, Wiley Online Library on [12/06/2025]. See the Terms and Conditions (https://onlinelibrary.wiley.com/terms-and-conditions) on Wiley Online Library for rules of use; OA articles are governed by the applicable Creative Commons License